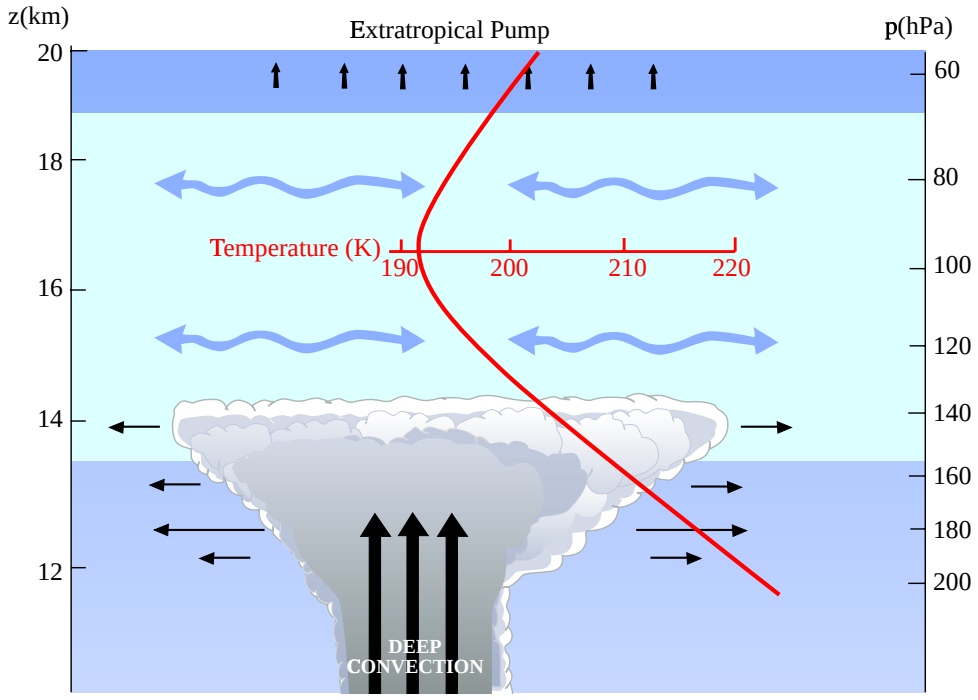

Figure 2.1 Schematic diagram of the hypothesized TTL (Tropopause Transition Layer), denoted by the pale blue region between ∼13.5 km and ∼19 km. Deep convection is shown penetrating the bottom of the TTL. Transport within the TTL is characterized by input of air mixed across the subtropical tropopause driven primarily by tropospheric weather systems (e.g., the summer monsoons), by quasi-horizontal mixing with extra-tropical stratospheric air, and by slow ascent to the overworld (the region where all isentropes exist solely in the stratosphere). J. R. Holton, private communication, 2000.

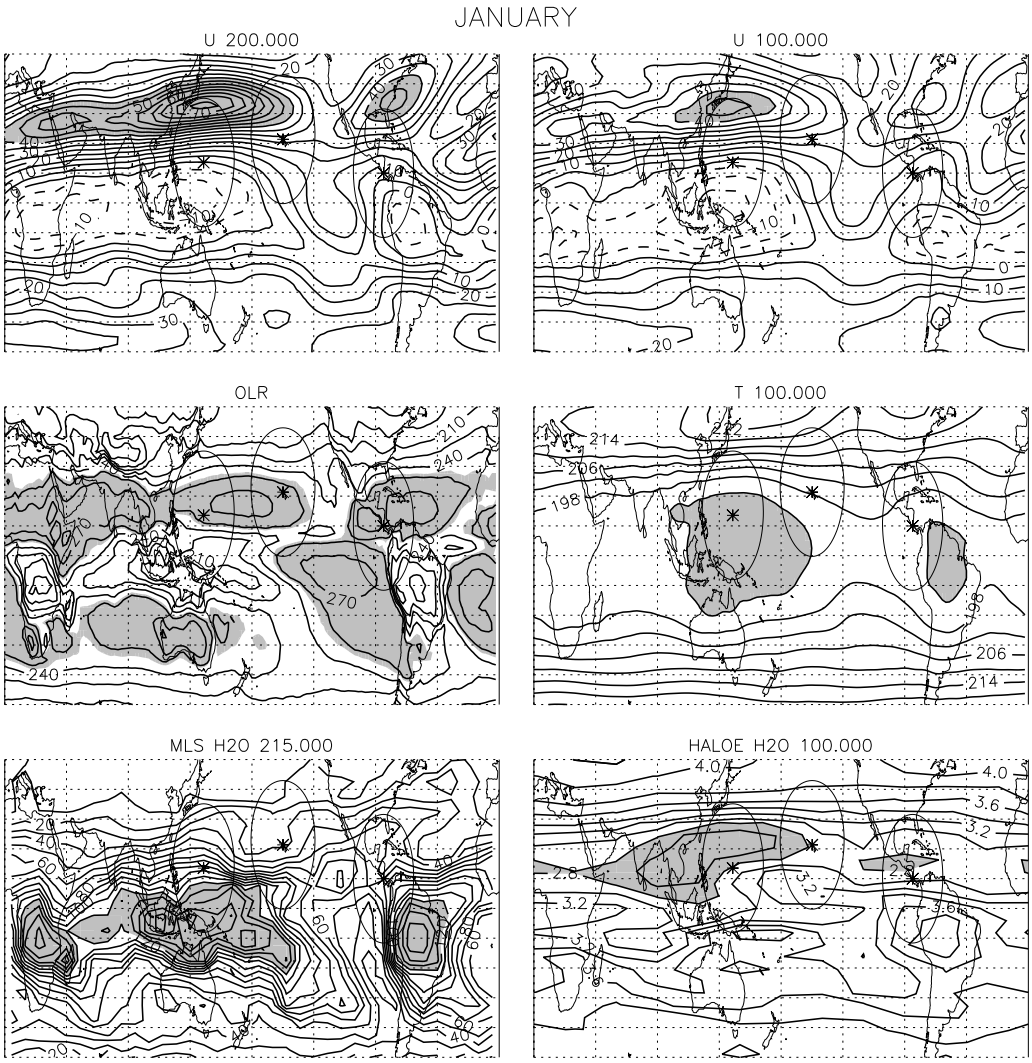

Figure 2.2 Climatogical values for January of: *Top* – calculated eastward component of velocity at 200 and 100 mbar; *Middle* – calculated outgoing longwave radiation (OLR) and analyzed temperature at 100 mbar; *Bottom* – mixing ratio of H_2O at 215 mbar measured by MLS and mixing ratio of H_2O at 100 mbar measured by HALOE. The meteorological data are derived from NCEP/NCAR reanalysis fields, the OLR values are from the NOAA-CIRES Climate Diagnostics Center, the MLS water vapor climatology is from Stone *et al.* (2000), and HALOE water vapor climatology is from Randel *et al.* (2000). P.A. Newman and D. W. Waugh, private communication, 2000.

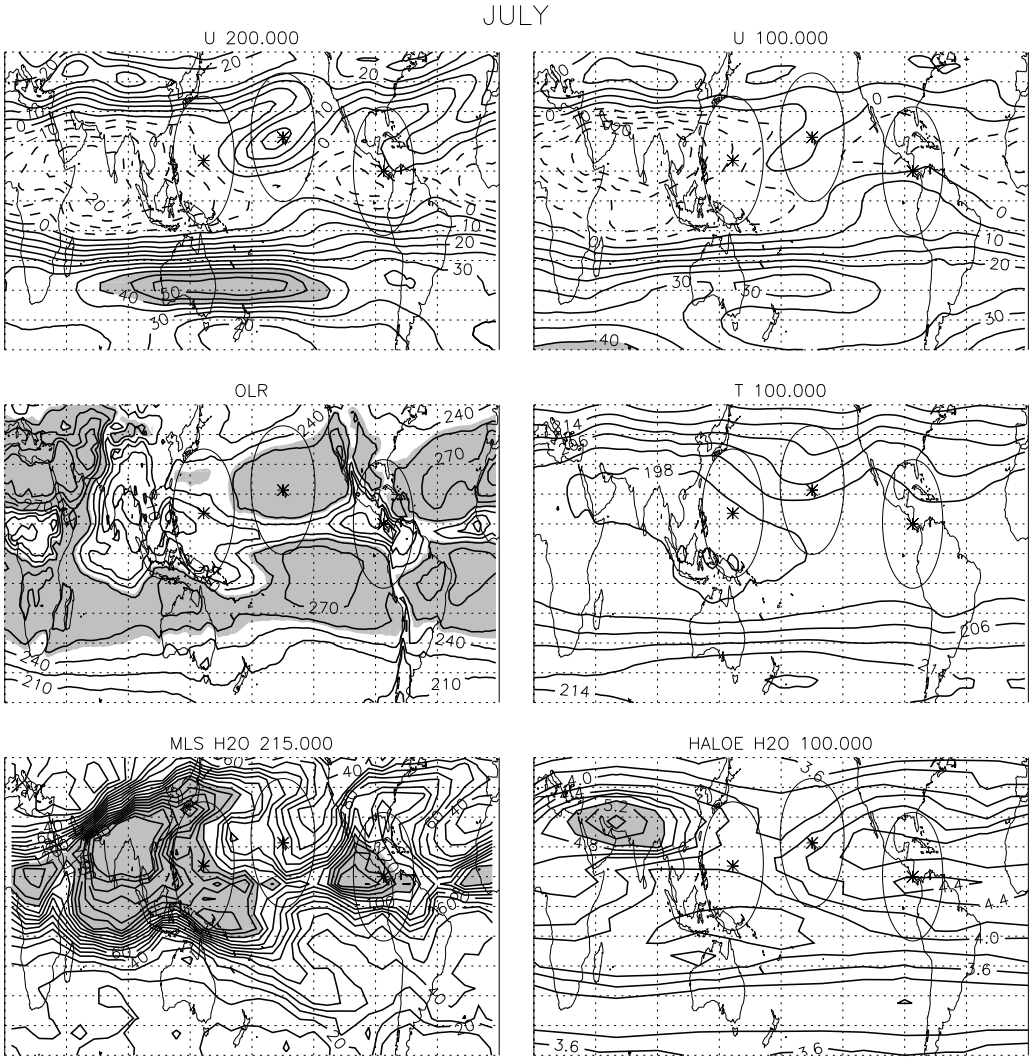

Figure 2.3 Climatogical values for July of: *Top* – calculated eastward component of velocity at 200 and 100 mbar; *Middle* – calculated outgoing longwave radiation (OLR) and analyzed temperature at 100 mbar; *Bottom* – mixing ratio of H_2O at 215 mbar measured by MLS and mixing ratio of H_2O at 100 mbar measured by HALOE. The meteorological data are derived from NCEP/NCAR reanalysis fields, the OLR values are from the NOAA-CIRES Climate Diagnostics Center, the MLS water vapor climatology is from Stone *et al.* (2000), and HALOE water vapor climatology is from Randel *et al.* (2000). P.A. Newman and D. W. Waugh, private communication, 2000.

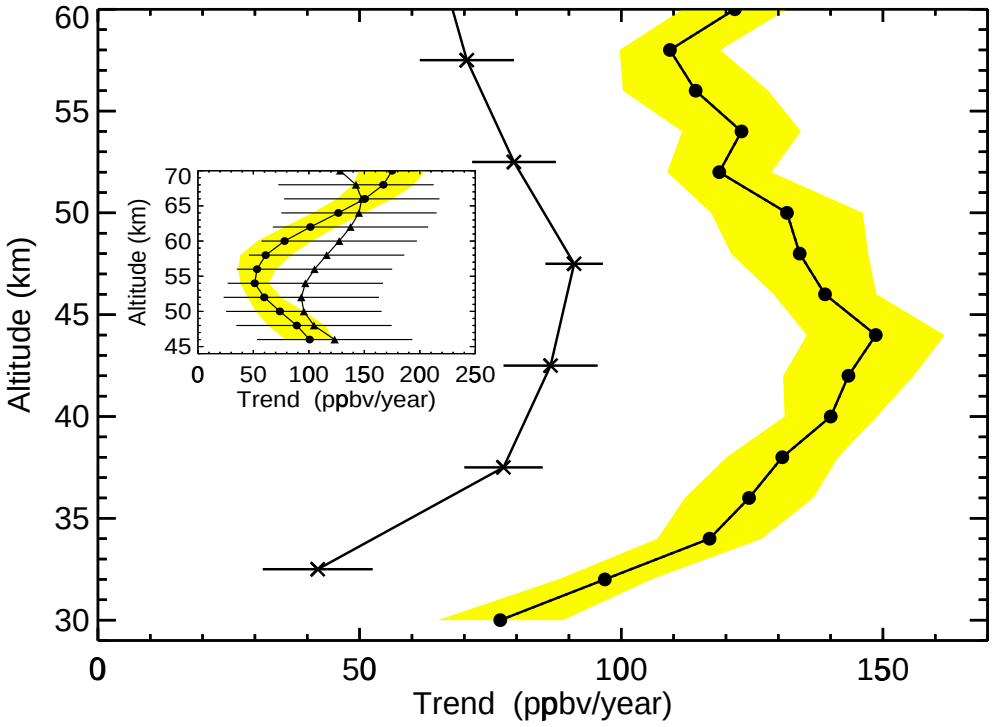

Figure 3.1 Global average linear trends in upper stratospheric water vapor derived from HALOE Version 18 observations by Evans *et al.* (1998) for 1992 to 1996 inclusive (crosses) and by Nedoluha *et al.* (1998) for September 1991 to February 1997 (circles). The insert shows a comparison of the trend for H_2O between May 1993 and October 1997 measured by a ground based microwave spectrometer at Table Mountain, California (34.4°N, 242.3°E) (triangles) to the HALOE trend for coincident measurements (Nedoluha *et al.*, 1998). The primary difference between the trends for H_2O found by Evans *et al.* and Nedoluha *et al.* is due to the statistical technique (e.g., model of the QBO) used to estimate the linear component of the nonlinear H_2O time series. From Chapter 6, WMO 1999 (see chapter for a description of the error bars).

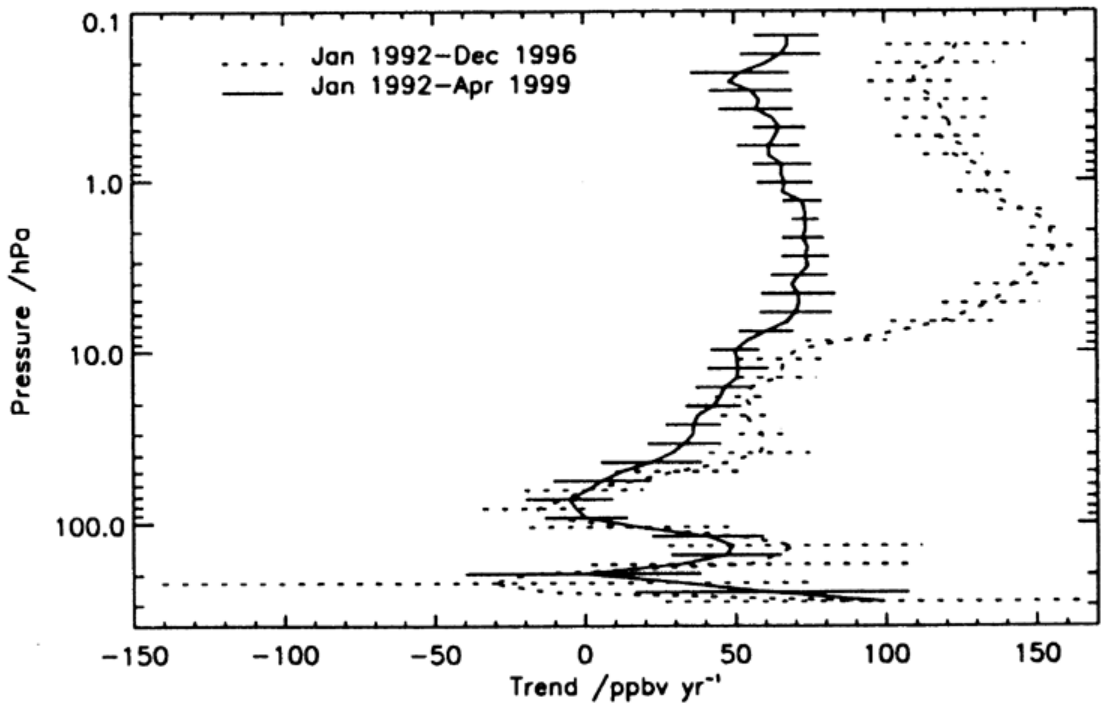

Figure 3.2 Globally and annually averaged water vapour trends dervied from zonal, monthly mean averages of Version 19 HALOE data for two time periods, as indicated. Error bars are two standard deviations estimates of the uncertainty. From Smith *et al.*, *GRL*, **27**, 1687, 2000.

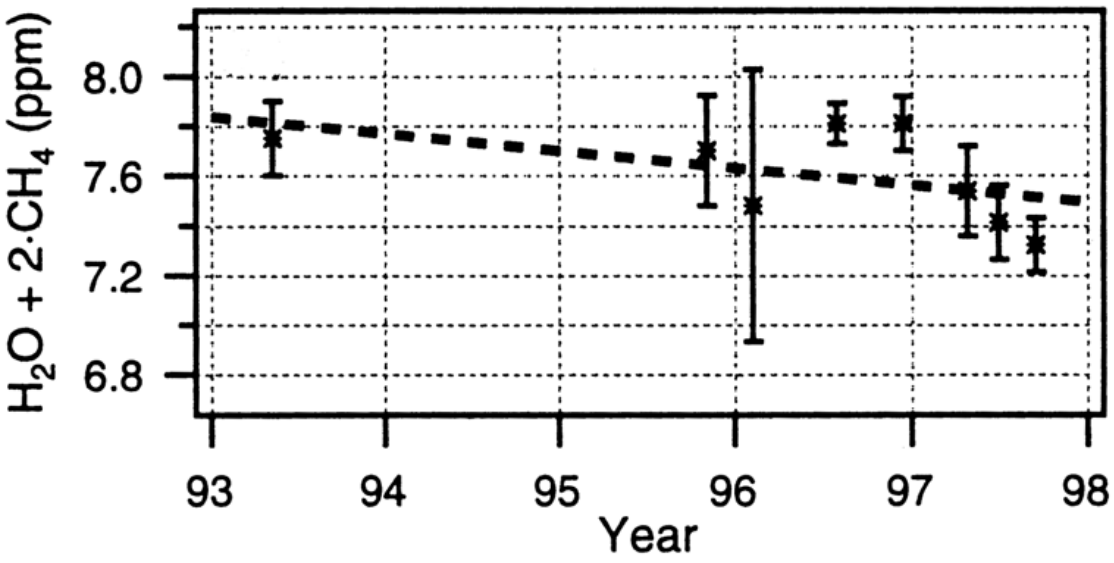

Figure 3.3 Mean value of H_2O+2CH_4 in the NH lower stratosphere for each deployment of SPADE (1993), STRAT (1995-1996), and POLARIS (1997), filtered by CH_4<1450 ppb (to target "aged" air masses). Data meeting the filter criterion were collected predominantly between latitudes of 40° and 90°N and potential temperatures of 470 and 540 K. The figure shows measurements of H_2O from the Harvard instrument and of CH_4 from the NOAA ACATS instrument on board the ER-2. The slope and 80% confidence of the slope is -0.07 ± 0.08 ppm yr^{-1}, indicating no significant trend in H_2O+2CH_4 during 1993 to 1997. This study also reported a lack of seasonal cycle for H_2O+2CH_4 in these "aged" air masses. From Hurst *et al.*, *JGR*, **104**, 8191, 1999.

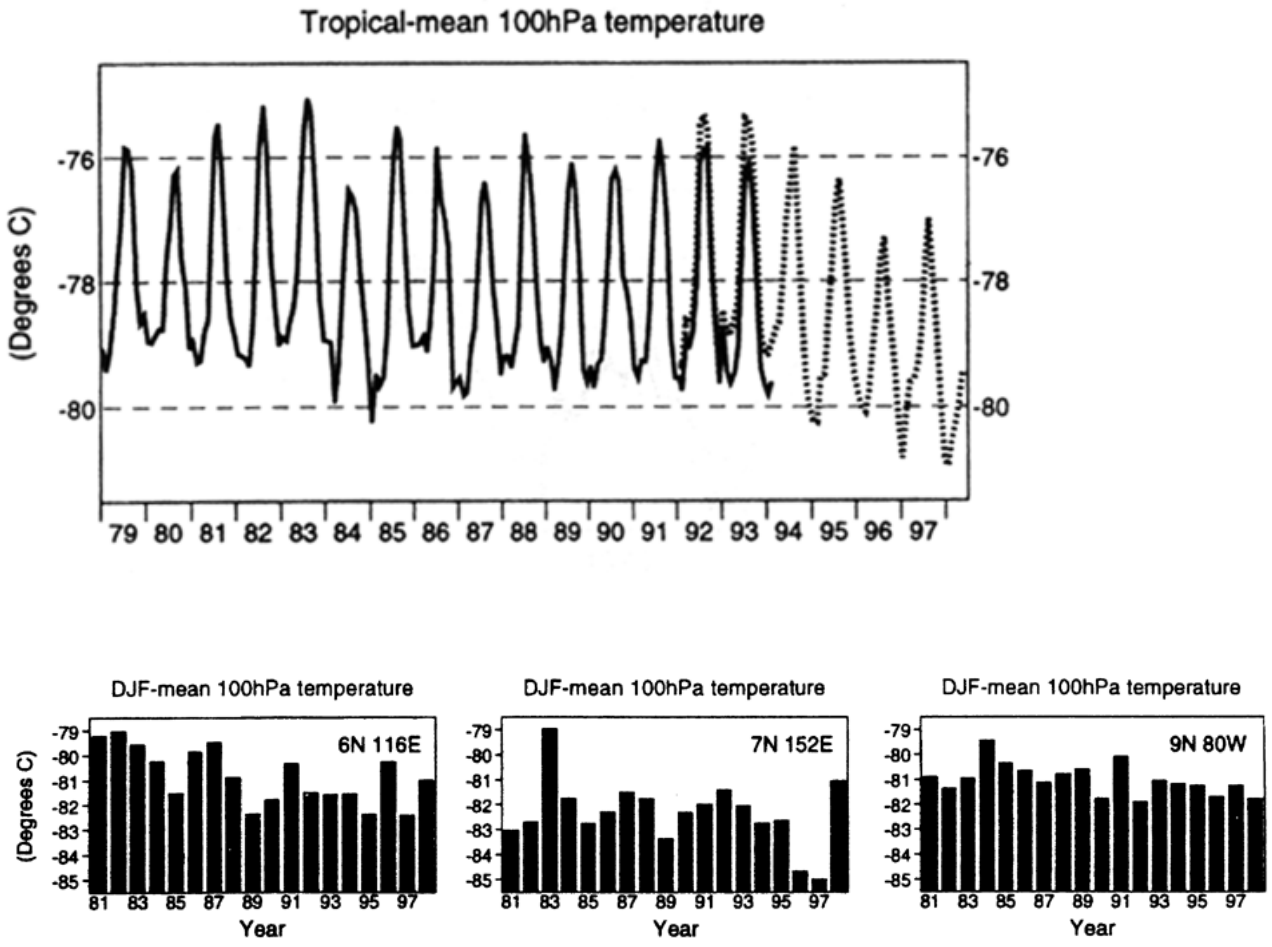

Figure 3.4 *Top Panel.* Tropical mean 100 hPa temperatures averaged at 1200 UTC for each month from January 1979 to May 1998. The solid line is computed from ECMWF reanalyses for the period up to February 1994. The dotted line is from the operational analyses for the period since January 1992. ***Bottom Panels.*** Time series of 100 hPa radiosonde temperatures for December-February at Kota Kinabalu (6°N, 116°E), Truk (7°N, 152°E), and Panama (9°N, 80°W) from 1980/81 (labelled 81) to 1997/98. From Simmons *et al.*, *QJRMS*, **125**, 353, 1999.

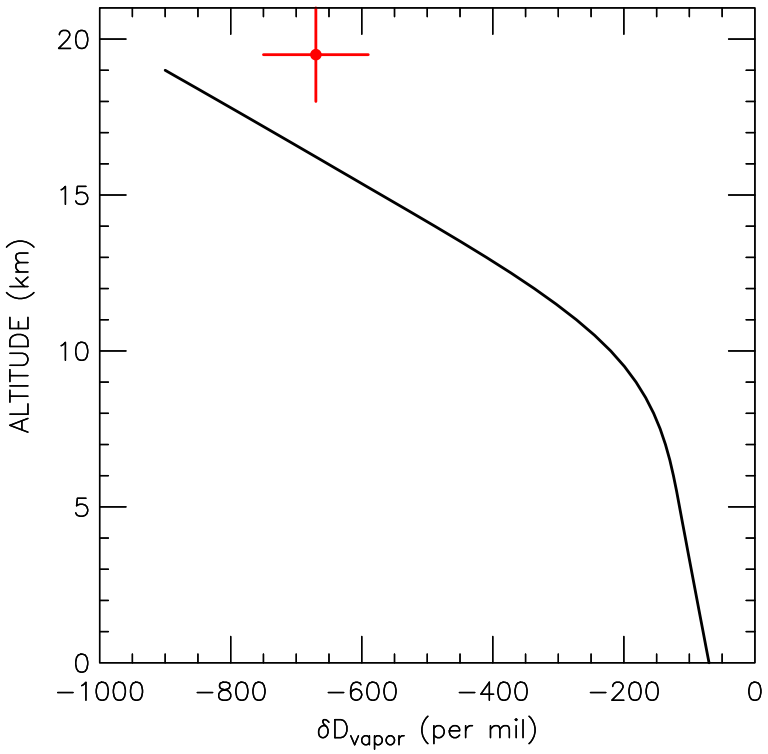

Figure 3.5 Measured value of δD (red point) of stratospheric water, after correction for minor contribution from oxidation of heavy methane (CH_3D), measured in the trpical lower stratosphere by ATMOS during November 1994. The horizontal error bar represents the standard deviation of the mean; the vertical error bar denotes the altitude range of the observations. The solid curve shows the calculated value for δD for conditions of thermodynamic equilibrium, desiccation to observed levels of stratospheric aridity, and no transport of condensate across the tropopause. From Moyer *et al.*, *GRL*, **23**, 2385, 1996.

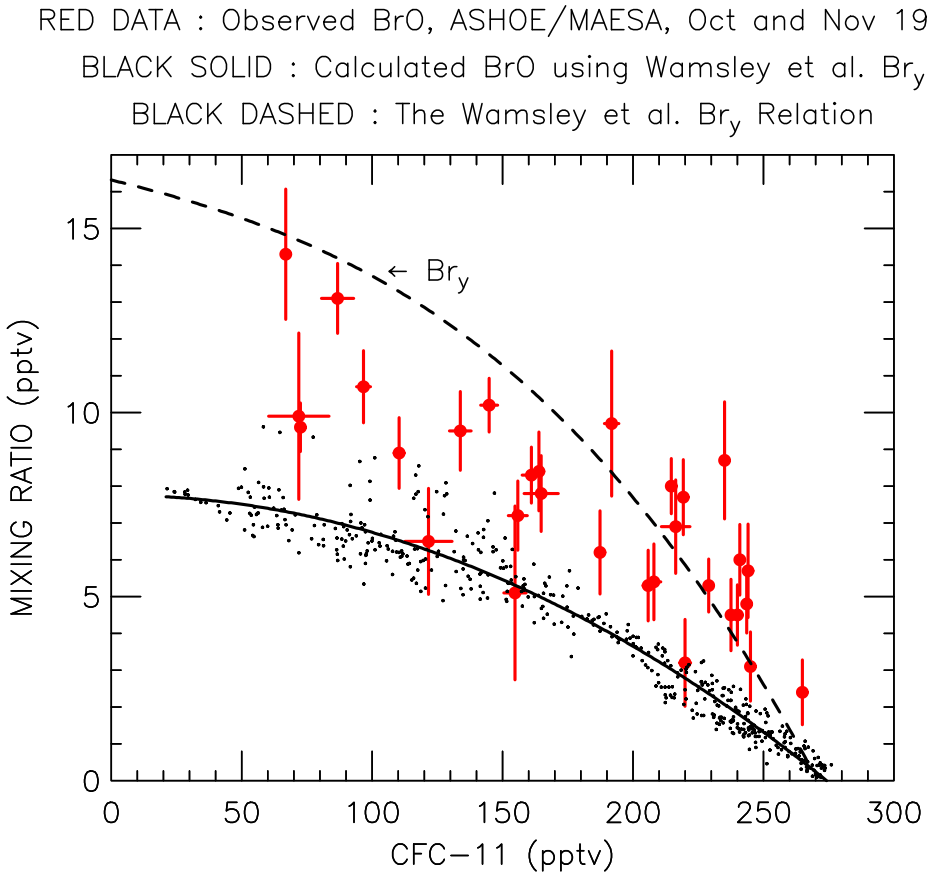

Figure 4.1 Observed mixing ratio of BrO vs CFC-11 in the lower stratosphere at mid-day during October and November 1994 (Wamsley *et al.*, 1998) (red points with error bars) and the calculated mixing ratio of BrO for the SZA, abundance of O_3, NO_y, etc. along the track of each flight. The solid curve is a fit to the model simulations. The dashed curve illustrates the Wamsley et al. (1998) Br_y relation used to constrain the model. This comparison is similar to Figure 7 of Wamsley *et al.* (1998), which illustrated that Br_y inferred from observed BrO substantially exceeds Br_y inferred from measured organic bromine source gases. R. J. Salawitch, private commuication, 2000.

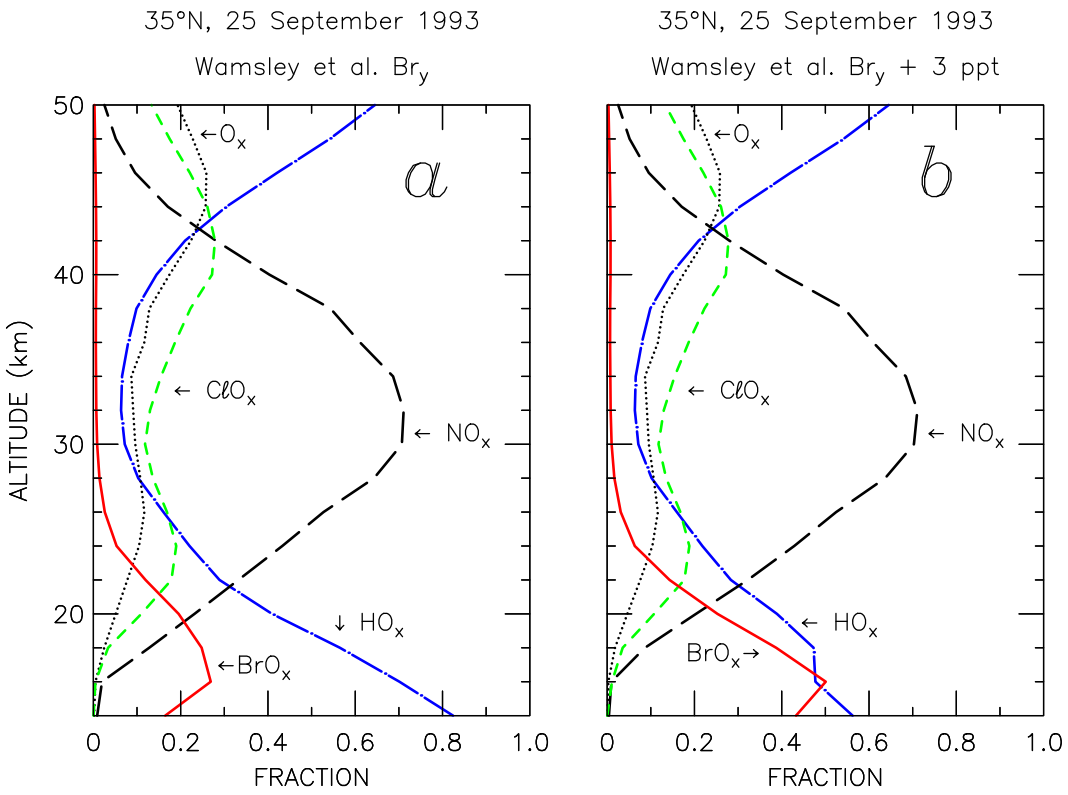

Figure 4.2 Calculated contribution to 24 hour average ozone loss from the various chemical families for a model constrained by MkIV observations of O_3 and radical precursors at mid-latitude (e.g., Sen *et al.*, 1998) for two different assumptions regarding Br_y: panel (*a*) – the Wamsley *et al.* (1998) relation; panel (*b*) – the Wamsley *et al.* (1998) relation + 3 pptv of Br_y. Reaction rates and absorption cross sections from JPL 00-3. R. J. Salawitch, private communication, 2000.

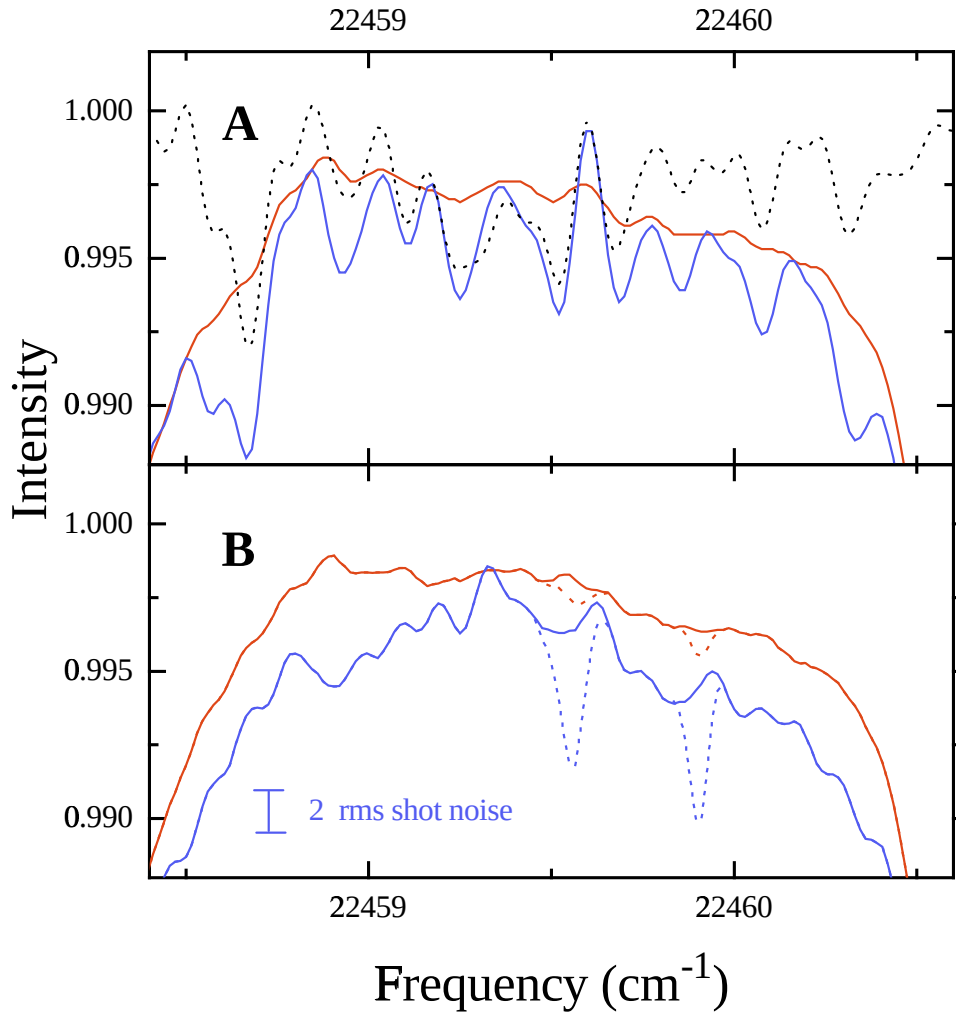

Figure 4.3 The solar spectrum measured at Kitt Peak for SZA=60° (red) and SZA=88° (blue) on 3 March 1994. Panel A. The black line shows the NO_2 laboratory absoprtion spectrum at $T = 240\,K$ and $p = 8\,mbar$; absorption due to NO_2 is clearly seen in both the high and low air mass spectra. Panel B. Residuals after removing the signature due to NO_2 (solid) are small, close to the shot noise limit for the instrument. The expected absorption due to IO if 1 pptv of inorganic iodine had been present in the stratosphere is shown by the dotted blue line. These measurements were used to deduce a stratospheric mixing ratio for total inorganic iodine of $0.2^{+0.3}_{-0.2}$ pptv. From Wennberg *et al.*, *JGR*, **102**, 8887, 1997.

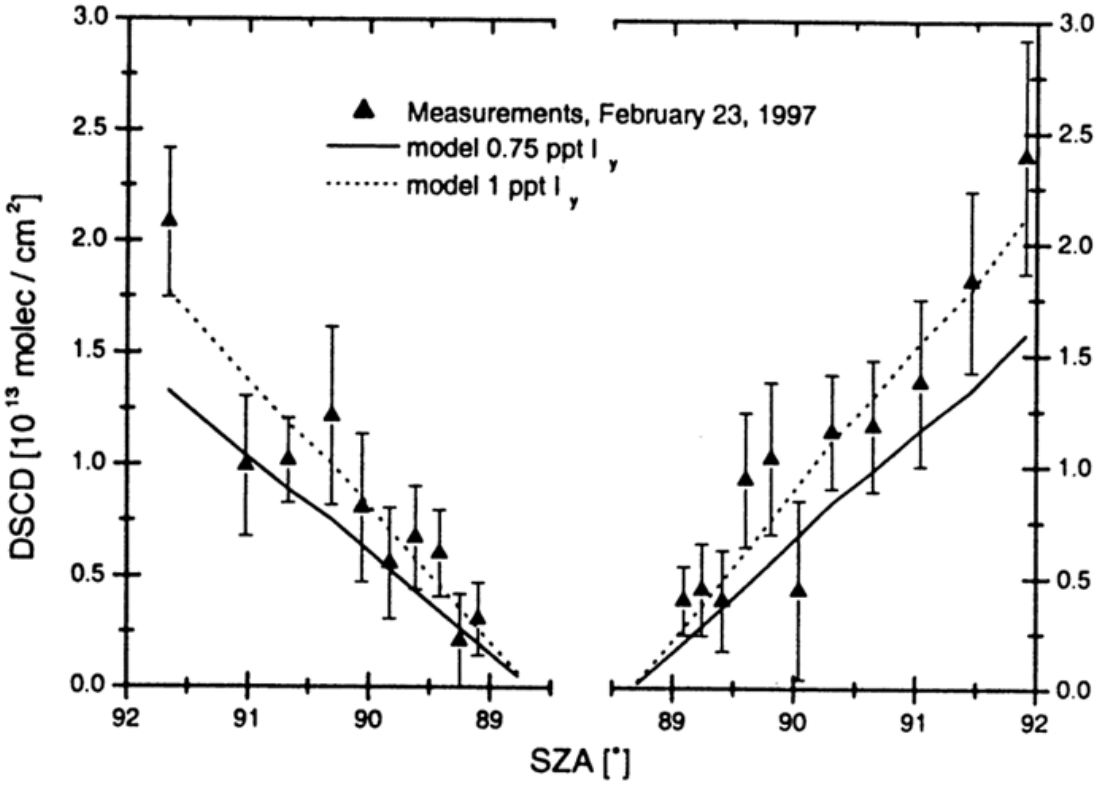

Figure 4.4 Differential slant column density (DSCD) of IO measured at Ny-Ålesund, Spitsbergen (79°N, 12°E) on 23 February 1997 during morning twilight (left) and evening twilight (right). The measurements were obtained using ground based spectrum between 425 to 461.5 nm recored with 0.9 nm wavelength resolution. A spectrum acquired at noon is used as background. The curves show the computed DSCD of IO assuming total stratospheric iodine of 1.0 pptv (dashed) and 0.75 pptv (solid). These observation have been used to estimate a stratospheric mixing ratio for IO of 0.65 to 0.80 ($\pm$0.2) pptv in polar spring 1997. From Wittrock *et al.*, *GRL*, **27**, 1471, 2000.

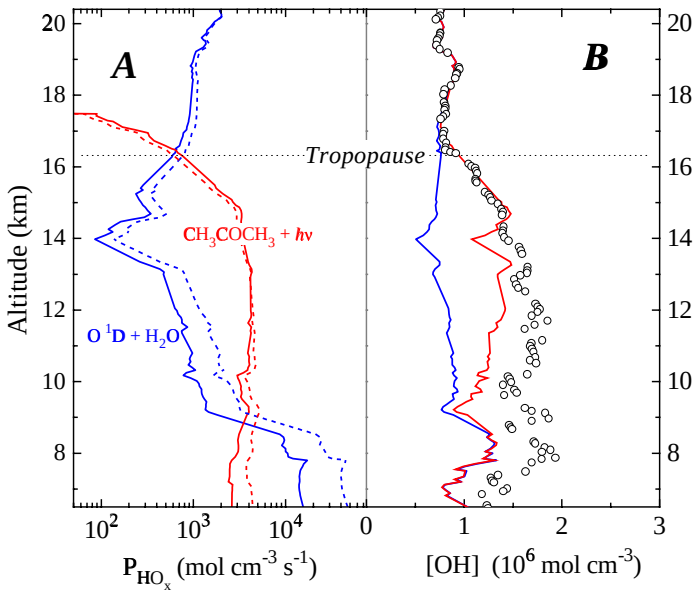

Figure 3

Figure 4.5 Profiles of the production rate of HO_x (Panel **A**) and concentration of OH (Panel **B**) on 7 November 1995 over Barber's Point, Hawaii (21°N, 158°W). The blue curves in Panel **A** show the production rate of HO_x from $O(^1D)+H_2O$ (solid: instantaneous; dashed, 24 hr average) based on measured O_3 and H_2O. Production of HO_x from $O(^1D)+H_2O$ drops by several orders of magnitude between 7 km and the tropopause. The red curves in Panel **A** show the production rate of HO_x from photolysis of acetone, which has been estimated based on measured correlations of acetone with CO from the DC-8 during the PEM-West B campaign. Between 12 km and the tropopause, measured concentrations of OH are underestimated by about a factor of 2 for a model that neglects acetone chemistry (blue curve, Panel **B**). Including the acetone source of HO_x in the model (red curve) leads to better agreement, but measured OH is still underestimated below 14 km. This underestimate may be due to improper estimates of the abundance of acetone or to the influence on HO_x of peroxides convected from the surface (*e.g.*, Jaegle *et al.*, 1997). From Wennberg *et al.*, *Science*, **279**, 49, 1998.

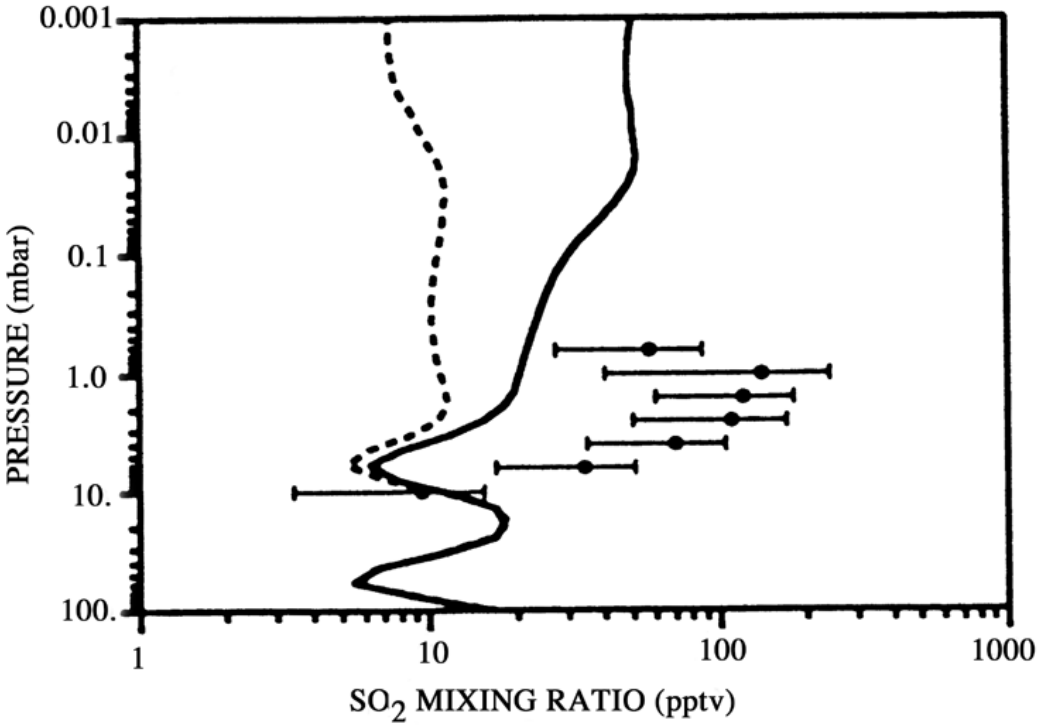

Figure 4.6 Observed profile (symbols with 1σ error bars) of SO_2 near 30°N during April-May 1985 by ATMOS (Rinsland *et al.*, 1995) and 2D model calculations of SO_2 assuming no photolysis of H_2SO_4 (dashed line) and a measured upper limit for the photolysis rate of H_2SO_4 (solid line). From Burkholder *et al.*, *GRL*, **27**, 2493, 2000.

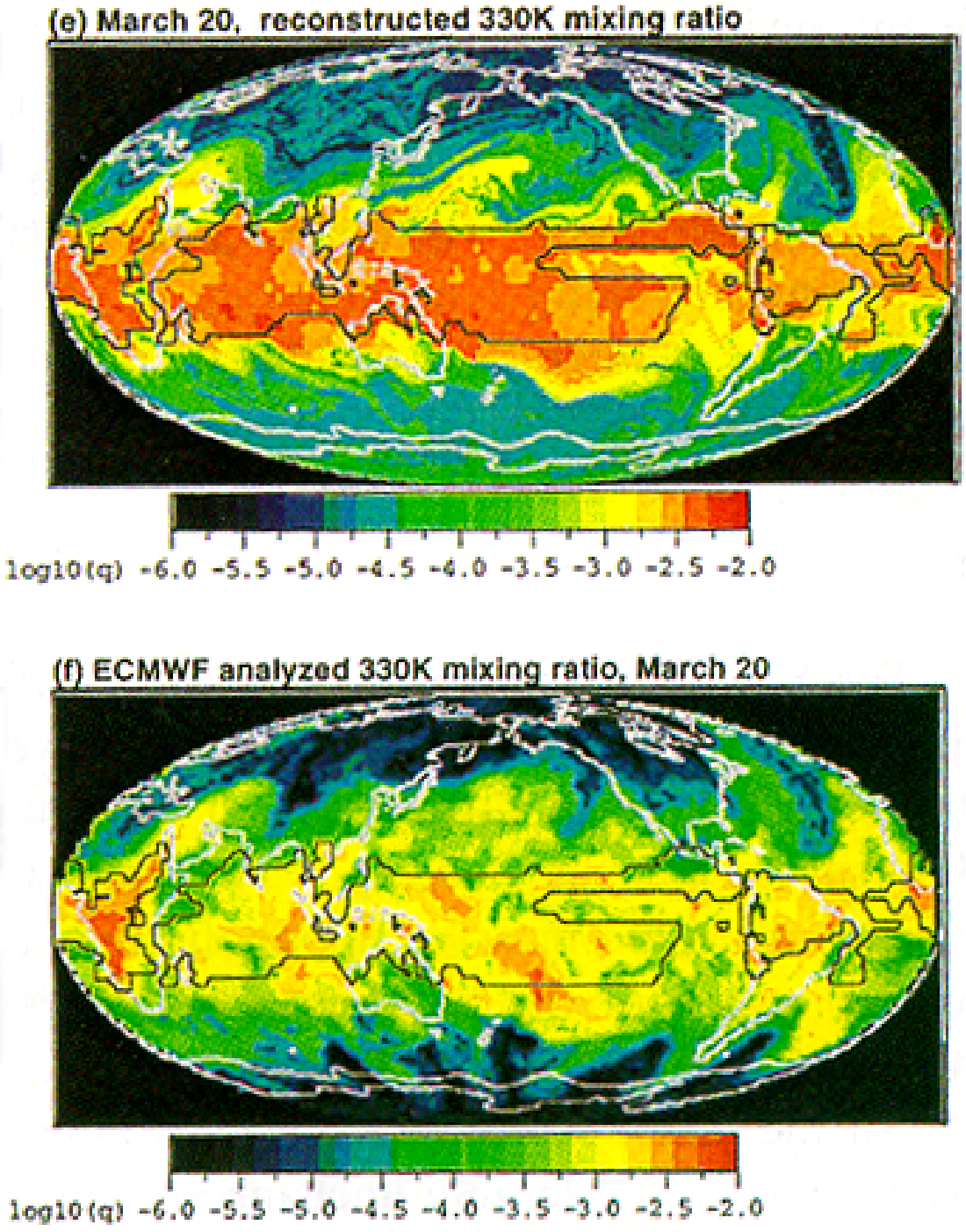

Figure 5.1 *Top Panel*: Calculated mixing ratio of H_2O on the 330 K potential temperature surface for 20 March 1993 based on a back-trajectory method that follows air parcels from the region of convection into the subtropics. Computed mixing ratios correspond to the minimum value of *local saturation mixing ratio* along the back-trajectory. ***Bottom Panel***: observations of the mixing ratio of H_2O at 330 K for 20 March 1993 based on ECMWF-analyzed moisture fields. The time period of analysis corresponds to the Central Equatorial Pacific Experiment (CEPEX). These simulations are used to argue that large scale advective mixing is a viable source of subtropical tropospheric water vapor. From Pierrehumbert *et al.*, *GRL*, **25**, 151, 1998.